



HAL
open science

Sigma coordinate pressure gradient errors: evaluation and reduction by an inverse method.

F. Auclair, Patrick Marsaleix, C. Estournel

► **To cite this version:**

F. Auclair, Patrick Marsaleix, C. Estournel. Sigma coordinate pressure gradient errors: evaluation and reduction by an inverse method.. *Journal of Atmospheric and Oceanic Technology*, 2000, 17, (-), pp.1348-1367. 10.1175/1520-0426(2000)0172.0.CO;2 . hal-00160519

HAL Id: hal-00160519

<https://hal.science/hal-00160519>

Submitted on 23 Feb 2023

HAL is a multi-disciplinary open access archive for the deposit and dissemination of scientific research documents, whether they are published or not. The documents may come from teaching and research institutions in France or abroad, or from public or private research centers.

L'archive ouverte pluridisciplinaire **HAL**, est destinée au dépôt et à la diffusion de documents scientifiques de niveau recherche, publiés ou non, émanant des établissements d'enseignement et de recherche français ou étrangers, des laboratoires publics ou privés.

Sigma Coordinate Pressure Gradient Errors: Evaluation and Reduction by an Inverse Method

F. AUCLAIR, P. MARSALEIX, AND C. ESTOURNEL

Laboratoire d'Aérodynamique, UMR CNRS/UPS 5560, Observatoire Midi-Pyrénées, Toulouse, France

(Manuscript received 24 February 1999, in final form 27 September 1999)

ABSTRACT

Sigma coordinate models currently suffer from the difficulty encountered in specifying the horizontal pressure gradient. Most of the efforts to reduce this truncation error lead to the loss of at least one integral constraint in the pressure gradient scheme (energy, tracer balance, etc.). Starting from a usual Arakawa-based scheme, it is shown that judicious adjustment of the sigma surfaces together with control of the bottom topography slope parameter and an "optimal modification" of the measured initial pressure field lead to a drastic reduction in the truncation errors. The first experiment is based on a coastal academic domain in order to compare the results of the proposed inverse method with published data. A few experiments are then conducted on the eastern part of the Gulf of Lions in the Mediterranean using data from the Suivilion experiment.

1. Introduction

Terrain-following coordinates (σ) are now widely used in the oceanographic community, and more specifically in coastal oceanography (see, e.g., Blumberg and Mellor 1987; Marsaleix et al. 1998). Compared to z -coordinate models, the σ formulation offers a much better representation of the effect of topography and several σ levels can be dedicated to the description of the bottom and surface layers (Gerdes 1993; Beckman 1998). However, Haney (1991) listed serious restrictions to their generalization, among which could be found the increased diapycnal diffusion or truncation errors linked to the horizontal pressure gradient numerical scheme. The specification of horizontal diffusion can indeed be troublesome, and a spurious increased diffusion along σ levels can introduce artificial current and static instabilities (Beckmann and Haidvogel 1993). Important contributions to this problem have lately been made by Beckman and Haidvogel (1997) and Barnier et al. (1998), but so far, it remains unsolved, and in the words of Mellor et al. (1998) it is still "endemic to all models." Yet, the use of a nonlinear stretched sigma coordinate (Song and Haidvogel 1994) or a "two-fold sigma coordinate system" (Beckers 1995) can noticeably reduce spurious diapycnal diffusion by avoiding large vertical variations of sigma surfaces in the pycnocline.

On the other hand, the problem of the specification of the horizontal pressure gradient has for a long time been widely documented in the atmospheric community (Corby et al. 1972; Arakawa and Suarez 1983), and various approaches have been employed to reduce these so-called truncation errors. Gary (1973) proposed to reduce their magnitude by subtracting a background density profile. This gives quite good results if the density profile does not vary too much over the domain, that is, if the horizontal extension of the domain is small enough. Another solution can be the use of higher-order schemes for the pressure gradient: fourth- and sixth-order schemes have, for instance, been proposed (McCalpin 1994; Chu and Fan 1997). More recently, Mellor et al. (1994, hereafter referred to as MEO) evaluated the magnitude of the truncation error and showed that the spurious geostrophic currents were advectively eliminated after several months of integration. For the academic case studied, they showed that the spurious geostrophic current could be as high as 7 cm s^{-1} after a 90-day diagnostic spinup. However, after 2 yr of prognostic integration, the current was reduced to only 0.2 cm s^{-1} . The author proposes in particular to run the model for a spinup time in order to adjust the density gradient and cancel out the horizontal pressure gradient truncation error.

Both types of errors, the increase in diapycnal diffusion and truncation errors, are thus fundamentally different. The first type can be seen as a "dynamic" error, in so far as its spurious impact on the quality of model results increases as time goes past, whereas the second one is more "static": the geostrophic current is already misrepresented in the initial field but the error slowly

Corresponding author address: Dr. Francis Auclair, Laboratoire d'Aérodynamique UMR CNRS/UPS 5560, Observatoire Midi-Pyrénées, 14, Av. E. Belin, 31400 Toulouse, France.
E-mail: aucf@aero.obs-mip.fr

decreases though the pressure field itself has been contaminated.

The fact is that the truncation error is only one part of the problem and the numerical scheme for the hydrostatic equation cannot be chosen solely on the basis of pressure gradient accuracy arguments. Integral constraints, such as energy, must also be balanced in the model (Arakawa and Suarez 1983), and the pressure gradient scheme must be associated with the corresponding advective scheme in order to preserve the energetic consistency of the model. Gerdes (1993) acknowledges that “efforts to reduce this error in a σ model necessarily involve the abandonment of one or more integral constraints” (conservation of tracers, conservation of energy, etc.). For instance, higher-order numerical schemes (McCalpin 1994; Chu and Fan 1997) must be associated with the corresponding advective scheme. This eventually leads to difficulties in tracer equations.

As a consequence, we chose to study the truncation error problem for a classic horizontal pressure gradient numerical scheme. To reduce these errors, the sigma surface distribution is adapted both to a classic density profile in the area and to the topography, and the pressure field is optimized by an inverse method in order to approach the “true” geostrophic field.

In the present paper we show that the slope factor, the sigma surface distribution, and finally the measured density and surface elevation fields can be initially adjusted in order to reduce the truncation error and to give the observed geostrophic current and Brunt–Väisälä frequency with a satisfactory accuracy. To optimally adjust the density and surface elevation fields, an inverse method is described in section 2, and is applied to a classic formulation of pressure (Arakawa and Suarez 1983). This initial adjustment of the known initial conditions is particularly useful for short-term integrations of the coastal ocean model.

MEO’s experiment is reviewed in order to evaluate the amplitude of the truncation errors produced by the Arakawa-based scheme and their reduction by the inverse method. Geostrophic currents are then evaluated in the framework of the Suivilion experiment in the Gulf of Lions (Durrieu de Madron and Panouse 1996) and the impact of both the twofold sigma coordinate system (Deleersnijder and Beckers 1992) and the proposed inverse method are investigated in detail.

2. Formulation of the free-surface pressure gradient

a. Horizontal pressure gradient

The model used is the coastal free-surface model Symphonie (Estournel et al. 1997; Marsaleix et al. 1998). This model is based on a mode-splitting approach (Blumberg and Mellor 1987) and the 3D primitive equations are discretized on a staggered C grid (Arakawa

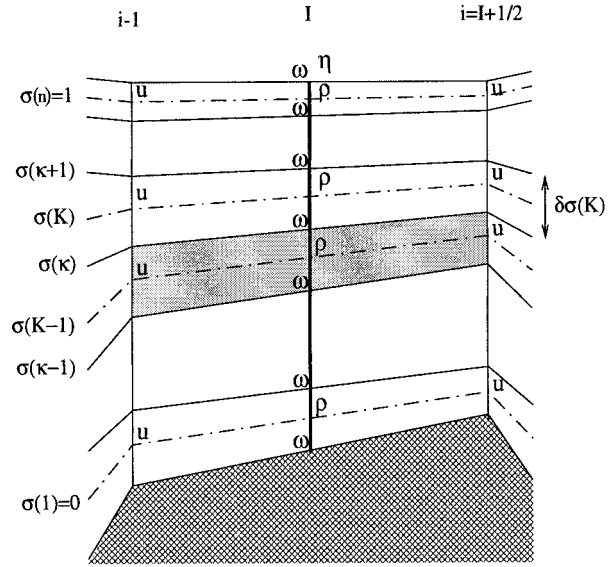


FIG. 1. Vertical section of the staggered σ C-grid at point (I, J) . Here K stands for σ surfaces, and k for interface surfaces.

and Lamb 1977) (Fig. 1). Hereafter we shall refer to the model in a compact form:

$$\mathbf{x}^f(t_{i+1}) = \mathbf{M}_i[\mathbf{x}^f(t_i)], \tag{2.1}$$

where \mathbf{x} is the model state vector and \mathbf{M} the dynamics operator. The notations are the classic notations given by Ide et al. (1997), in which the superscripts $f, t, a,$ and o stand, respectively, for forecast, true, analysis, and observation.

Of interest is the formulation of the horizontal pressure gradient in sigma coordinates, and the diffusion is simply applied along the σ coordinates. Analytically, the horizontal pressure gradient can be written:

$$\frac{\partial P^*}{\partial x^*} = \frac{\partial P}{\partial x} + \frac{\partial \sigma}{\partial x^*} \frac{\partial P}{\partial \sigma}, \tag{2.2}$$

where (x^*, y^*, z) and (x, y, σ) are, respectively, the z and σ coordinates and are related to each other by

$$\begin{cases} x = x^* \\ y = y^* \\ \sigma = \frac{h + z}{h + \eta} \end{cases} \tag{2.3}$$

where $h = h(x, y)$ the ocean depth, and $\eta = \eta(x, y)$ the surface elevation anomaly. Here P^* stands for $P(x^*, y^*, z)$ and P for $P(x, y, \sigma)$. In Eq. (2.4) $\rho = \rho(x, y, \sigma)$ is the density field and ρ_0 a constant reference density ($\rho_0 = 1024.8 \text{ kg m}^{-3}$). Without any loss of generality, the derivatives are written hereafter with respect to x , the y derivative being derived the same way. The first term on the right-hand side of (2.2) is the “ σ -pressure gradient,” while the second term is sometimes re-

ferred to as the ‘‘hydrostatic correction.’’ We then introduce a perturbation density ρ' :

$$\rho(x, y, \sigma) = \rho_0 + \rho'(x, y, \sigma). \quad (2.4)$$

With these notations, the hydrostatic assumption can be written

$$\frac{\partial P^*}{\partial z} = -g\rho^*, \quad (2.5)$$

where $\rho^* = \rho(x^*, y^*, z)$.

Neglecting the variation in atmospheric pressure, this leads to the following expression for the horizontal pressure gradient in σ coordinates:

$$\frac{\partial P^*}{\partial x^*} = \Pi_I^x + \Pi_E^x, \quad (2.6)$$

where Π_I^x and Π_E^x are, respectively, the internal and external part of the pressure gradient:

$$\begin{aligned} \Pi_I^x &= \Pi^x(\sigma) - \int_0^1 \Pi^x(\sigma) d\sigma \quad \text{and} \\ \Pi_E^x &= \rho_0 g \frac{\partial \eta}{\partial x} + \int_0^1 \Pi^x(\sigma) d\sigma, \end{aligned}$$

with $\Pi^x(\sigma)$ given by

$$\begin{aligned} \Pi^x(\sigma) &= -\frac{\partial}{\partial x} g(h + \eta) \int_{\sigma}^1 \rho' d\sigma' - g(1 - \sigma)\rho' \frac{\partial h}{\partial x} \\ &\quad - g\sigma\rho' \frac{\partial \eta}{\partial x}. \end{aligned}$$

The classic numerical scheme by Arakawa and Suarez (1983) is chosen for the computation of (2.6) on the staggered C grid of the model. The horizontal pressure gradient thus reads for $K \in [1, N - 1]$,

$$\begin{aligned} \Pi_{i,J,K}^{\rho',\eta} &= \frac{\partial P}{\partial x^*}(i, J, K) \\ &= g \left[\frac{\delta\sigma_K}{2} \frac{\Delta[\rho'_k(h + \eta)]_{i,J}}{\Delta x} \right. \\ &\quad \left. + \sum_{K'=K+1}^N \delta\sigma_{K'} \frac{\Delta[\rho'_{K'}(h + \eta)]_{i,J}}{\Delta x} \right] \\ &\quad - g \left[(1 - \bar{\sigma}_K) \frac{\Delta h_{i,J}}{\Delta x} - \bar{\sigma}_K \frac{\Delta \eta_{i,J}}{\Delta x} \right] \tilde{\rho}'_{i,J,K} + g\rho_0 \frac{\Delta \eta_{i,J}}{\Delta x} \end{aligned} \quad (2.7)$$

for $K = N$:

$$\begin{aligned} \Pi_{i,J,K}^{\rho',\eta} &= \frac{\partial P}{\partial x^*}(i, J, K) \\ &= g \left[\frac{1}{2} \delta\sigma_K \frac{\Delta[\rho'_k(h + \eta)]_{i,J}}{\Delta x} \right] \\ &\quad - g \left[(1 - \bar{\sigma}_K) \frac{\Delta h_{i,J}}{\Delta x} - \bar{\sigma}_K \frac{\Delta \eta_{i,J}}{\Delta x} \right] \tilde{\rho}'_{i,J,K} + g\rho_0 \frac{\Delta \eta_{i,J}}{\Delta x}, \end{aligned} \quad (2.8)$$

with $\delta X_K = X_{k+1} - X_k$ for vertical variations, $\Delta X_{i,J} = X_{i,j+1} - X_{i,j}$ for horizontal variations in the x direction (Δx being the horizontal grid increment), and $\bar{X}_K = (X_{k+1} + X_k)/2$ for vertical averages and $\bar{X}_{i,J} = (X_{i,j+1} + X_{i,j})/2$ for horizontal averages in the x direction. Here N is the number of σ levels. Capital indices (I, J) are chosen for grid points, and lowercase indices (i, j) for interface grid points. Vertically, the same type of notation is used for σ surfaces (k) and interface σ surfaces (K). A complete description of the staggered C grid is also given in Fig. 1.

b. The σ -pressure gradient truncation error

The σ -pressure gradient and the hydrostatic correction being several orders of magnitude larger than their difference, the ‘‘numerical’’ expressions (2.7)–(2.8) can sometimes differ from the ‘‘true’’ pressure gradient. Careful observation of the way (2.7)–(2.8) are obtained leads to interesting conclusions on the possible distribution of σ levels. Indeed, Mesinger and Janjic (1985) show that the construction of the numerical scheme for the pressure gradient can be divided into three steps. First of all, the hydrostatic equation is integrated to obtain pressure P on σ surfaces at density points (I, J, K) and ($I + 1, J, K$) (Fig. 2). Then, the hydrostatic equation is used again to obtain the pressure at horizontal surfaces in the neighborhood of point (i, J, K) (points A and B on Figs. 2a and 2b). Last, the values of the pressure thus obtained are used to compute the pressure gradient at point (i, J, K) [horizontal velocity point in the x direction (u)].

The density profile is thus approximated by a piecewise linear function of σ , which leads Mesinger and Janjic (1985), Haney (1991), and others to identify the so-called hydrostatic consistency problem. To be hydrostatically consistent, the numerical pressure gradient is supposed to use the same scheme for the hydrostatic equation in steps 1 and 2. In particular, for a staggered C grid, the scheme is shown to be hydrostatically consistent as long as points A and B of Fig. 2a are in the same σ layer as point (i, K). Figure 2b is an example of a hydrostatically inconsistent scheme. MEO suggest that hydrostatic consistency is not an additional limitation to the use of σ levels, but rather a particular case of the truncation error problem. In fact, the major difficulties appear in regions of sharp density gradients where the piecewise linear

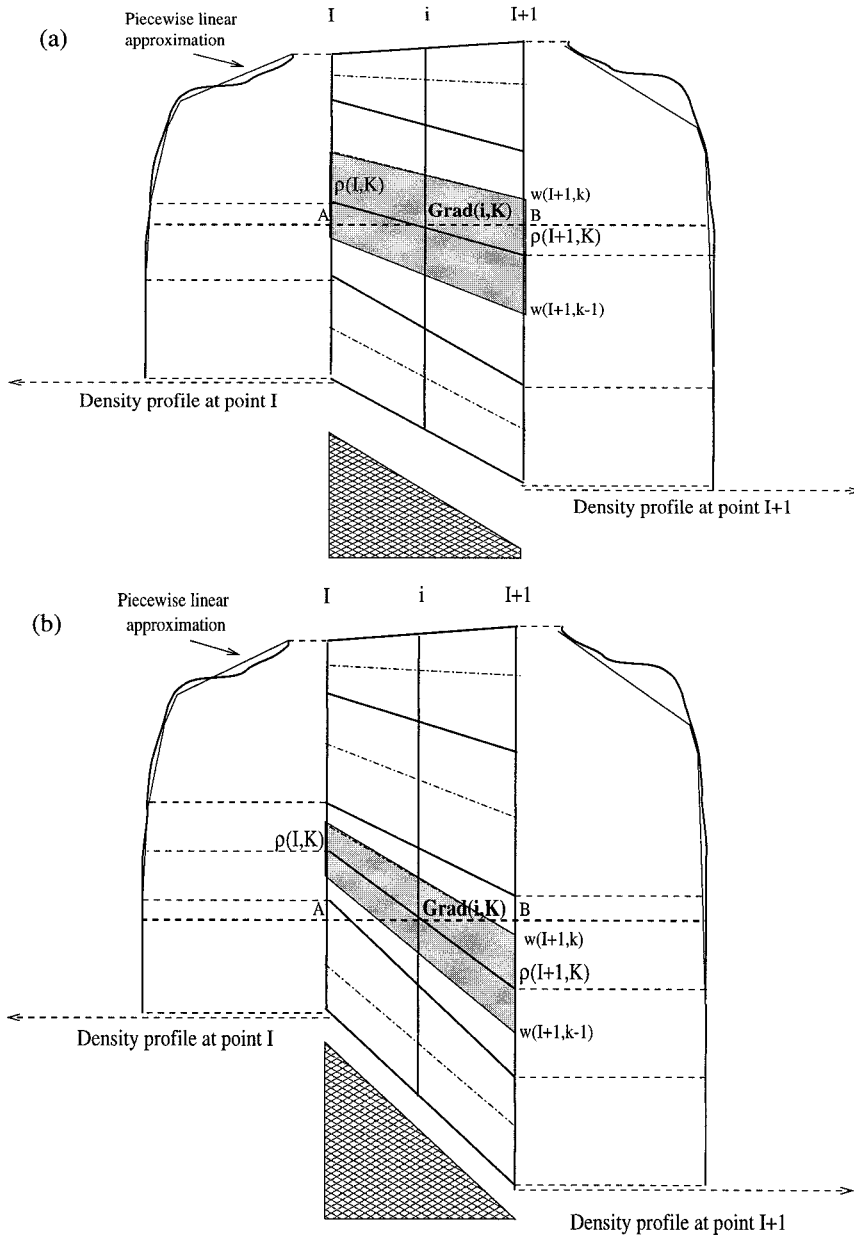


FIG. 2. Horizontal pressure gradient for a staggered C grid, piecewise linear approximation of the density profile: (a) hydrostatically consistent grid, (b) hydrostatically inconsistent grid.

approximation itself can be somewhat different from the “true” profile. Sharp density gradients, if they are associated with variations in σ surfaces, lead to large “truncation” errors in the computation of the pressure gradient force. Different approaches can help. The only way to conserve horizontal σ levels inside the pycnocline in regions of sharp topography gradients seems to be the use of a twofold σ -coordinate system (Deleersnijder and Beckers 1992). It is shown in section 4 that a constant upper fold provides a good resolution just below the surface where most physical processes are likely to take place, but also prevents the crossing of iso- σ surfaces

with iso-density surfaces, which significantly reduces the truncation errors.

A few interesting observations can also be made by expanding the pressure gradient force with respect to σ . In the neighborhood of point z_0 , the density can be written

$$\rho(x, y, z) = \rho(x, y, z_0) + \frac{\partial \rho}{\partial z}(x, y, z_0)[(1 - \sigma)h(x, y) - z_0] + \dots \tag{2.9}$$

Substituting (2.9) into (2.7), we obtain the complete expression for the truncation error (first order):

$$\begin{aligned} \Pi_{i,j,k}^n - \Pi_{i,j,k}^t &= \frac{g}{2} \frac{\Delta(\alpha h^2)_{i,j}}{\Delta x} [(1 - \sigma_k)^2 - (1 - \bar{\sigma}_k)^2] \\ &\quad - \frac{g(1 - \bar{\sigma}_k)^2}{2} \frac{\Delta(\alpha)_{i,j}}{\Delta x} (h_{i,j} h_{i+1,j} - h_{i,j}^2), \end{aligned} \quad (2.10)$$

where

$$\alpha = \frac{\partial \rho}{\partial z}(x, y, z_0),$$

and for the analytical profile (2.9),

$$\Pi_{i,j,k}^t = -\frac{g(1 - \bar{\sigma}_k)^2}{2} \frac{\Delta(\alpha)_{i,j}}{\Delta x} h_{i,j}^2.$$

For the present discussion, the terms

$$g(1 - \bar{\sigma}_k) \bar{\rho}'_{i,j,k} \frac{\Delta(\eta)_{i,j}}{\Delta x}$$

have been neglected in (2.10) as we can easily show that $|\bar{\sigma} \bar{\rho}' / \rho_0| < 10^{-3}$.

The zeroth-order terms all vanish because they only involve linear terms that cancel out. In fact, the truncation errors appear with the first “nonlinearity,” that is, the misrepresentation of the quadratic terms. Thus, at order 1, the errors result from the finite-difference analog of $(1 - \sigma)^2$ [first term in the right-hand side of (2.10)]. The computation of the second term also confirms the previous observation concerning the misrepresentation of nonlinear contributions, with the appearance of square terms in h . At order 2, lengthy computation shows that problems arise from both square and cubic terms, etc. The first term of the right-hand side of (2.10) is depth-independent if the σ levels are spaced uniformly in the vertical. Indeed, we can write:

$$\overline{(1 - \sigma_k)^2} - (1 - \bar{\sigma}_k)^2 = \left(\frac{\delta \sigma_k}{2} \right)^2. \quad (2.11)$$

This is consistent with the results obtained by Haney (1991), and he removes this term by considering only the difference from the mean density gradient. MEO also obtained a vanishing truncation error for a linear density profile by removing an area average density profile. However, this “first order” term leads to a spurious barotropic current that affects both the average depth density and the surface elevation anomaly of the free-surface model external mode. The second term in (2.10) is related to the x dependency of the density profile and vanishes for $\alpha = 0$. This leads to the conclusion that the truncation error for a given experiment cannot be fully evaluated by considering only a horizontally homogeneous profile.

MEO showed that the previous truncation error was advectively removed during a prognostic run and even-

tually vanishes after several inertial oscillations, the counterpart of this removal obviously being a modification of the density and surface elevation fields. The curl of the truncation error (2.10) does not normally vanish either and Mellor et al. (1998) showed that it leads to the appearance of a new type of error in the vorticity conservation equation, namely the “sigma error of the second kind.” They further showed that this error was not advectively removed and leads to small asymptotic values of the truncation error, which do not cancel out with respect to the geostrophic current.

c. Inverse method

Thus, the horizontal pressure gradient truncation error can lead to a spurious evaluation of the geostrophic components (u_g, v_g) of the current in regions of steep bottom topography gradients. In the present paper, recovering the geostrophic components is transformed into an optimal control problem: knowing the initial “true” geostrophic current, the optimal problem is to find the smallest disturbance of the pressure field (density and surface elevation anomaly) such that the horizontal pressure gradient truncation error is as small as possible. Yet, the adjustment of the pressure gradient is not sufficient to realistically define the density field, besides which the Brunt–Väisälä frequency of the density profile must also be considered. While the geostrophic component of general circulation can easily be evaluated from density observations, the direct computation of the Brunt–Väisälä frequency from observations is much more difficult: the vertical derivative of the density is very sensitive to observation noise. Thus, the Brunt–Väisälä frequency is computed from the interpolated density field itself, and we require that the adjustment of the geostrophic component does not lead to any major changes in this frequency.

Before the analysis, the initial density anomaly (ρ') and surface elevation (η) are given by the multivariate “background or first guess vector” $\mathbf{x}^b(t_0)$:

$$\mathbf{x}^b(t_0) = \begin{bmatrix} \rho^b(t_0) \\ \eta^b(t_0) \end{bmatrix}. \quad (2.12)$$

The analysis density and surface elevation fields after optimization are given by the multivariate “analysis” vector \mathbf{x}^a :

$$\mathbf{x}^a(t_0) = \mathbf{x}^b(t_0) + \delta \mathbf{x}(t_0), \quad (2.13)$$

where $\delta \mathbf{x}$ is the optimal perturbation. Let \mathbf{y}^o be the observation vector made of the geostrophic component of the general circulation and of the Brunt–Väisälä frequency of the interpolated density profile at $t = t_0$, that is, before the initialization of the coastal model \mathbf{M} and \mathbf{H} the observation operator that gives the geostrophic components and the Brunt–Väisälä frequency of the state vector $\mathbf{x}^a(t_0)$. Using the formulation of the hori-

zontal pressure gradient (2.7)–(2.8), the constraints of the optimal problem can now be written for $\delta\mathbf{x}$:

$$\mathbf{H}\mathbf{x}^a = \mathbf{H}(\mathbf{x}^b + \delta\mathbf{x}) = \mathbf{y}^o$$

$$\Leftrightarrow \begin{cases} -\frac{1}{\rho_0} \Pi_{i,j,K}^{\rho^b + \delta\rho, \eta^b + \delta\eta} = (f\mathbf{v}_{\text{geo}}^t)_{i,j,K} \\ -\frac{1}{\rho_0} \Pi_{l,j,K}^{\rho^b + \delta\rho, \eta^b + \delta\eta} = (-f\mathbf{u}_{\text{geo}}^t)_{l,j,K} \\ -g \frac{1}{\rho_0} \frac{(\delta\rho_{l,j,K+1} - \delta\rho_{l,j,K})}{\Delta z} = 0 \end{cases} \quad (2.14)$$

where (I, J, K) is a point of the model C grid, and for the last constraint $K \in [1, N - 1]$. The first two constraints are derived from the geostrophic current and the last one is related to the Brunt–Väisälä frequency. The “true” components of the geostrophic current ($\mathbf{u}_{\text{geo}}^t, \mathbf{v}_{\text{geo}}^t$) are given by the interpolation of the observed geostrophic current or by the geostrophic current from an ocean general circulation model.

The cost function associated with the previous optimal control problem is given by

$$J = \delta\mathbf{x}^T \mathbf{B}^{-1} \delta\mathbf{x} + [(\mathbf{y}^o - \mathbf{H}\mathbf{x}^b) - \mathbf{H}\delta\mathbf{x}]^T \mathbf{R}^{-1} [(\mathbf{y}^o - \mathbf{H}\mathbf{x}^b) - \mathbf{H}\delta\mathbf{x}]. \quad (2.15)$$

The perturbation $\delta\mathbf{x}$ is the control variable and \mathbf{B} and \mathbf{R} are the background and model covariance matrices. According to Gill (1982), the solution of the optimal problem can be written

$$\delta\mathbf{x}(t_0) = \mathbf{B}\mathbf{H}^T[\mathbf{H}\mathbf{B}\mathbf{H}^T + \mathbf{R}]^{-1}(\mathbf{y}^o - \mathbf{H}\mathbf{x}^b). \quad (2.16)$$

The computation of the covariance matrices is based on the values of slope parameter (r) and the specification of the maximum disturbance for density and surface elevation fields ($\delta\rho_{\text{max}}$ and $\delta\eta_{\text{max}}$). The background covariance matrix \mathbf{B} is written

$$\mathbf{B} = \mathbf{D}^{1/2} \mathbf{C} \mathbf{D}^{1/2}, \quad (2.17)$$

where \mathbf{C} is the matrix of the smoothing operator given by Wahba and Wendelberger (1980):

$$J_3(\Phi) = \sum_{\alpha_1 + \alpha_2 + \alpha_3 = 3} \frac{6}{\alpha_1! \alpha_2! \alpha_3!} \times \iiint \left(\frac{\partial^3 \Phi}{\partial x^{\alpha_1} \partial y^{\alpha_2} \partial z^{\alpha_3}} \right)^2 dx dy dz, \quad (2.18)$$

where J_3 is normalized so that the diagonal elements in \mathbf{C} are equal to one, and Φ is either the density or the surface elevation anomaly. Here \mathbf{D} and \mathbf{R} are the diagonal matrices containing the variance of the observations $[\sigma(\rho)$ and $\sigma(\eta)]$, and of the model (γ). As a first approximation, the variances are taken to be homogeneous and a small corrective nonhomogeneous term (10%) is inserted in \mathbf{D} to take into account the presence

of steep bottom topography gradients. This can be written

$$\mathbf{D}_{l,j,K} = [\sigma(\rho), \sigma(\eta)](1 + 0.1\|r\|_{l,j}). \quad (2.19)$$

For the present study, $\sigma(\rho) = 1$ and $\sigma(\eta) = 0.005$, and the slope parameter $r = (r_{l,j}, r_{i,j})$ is given on the C grid by

$$(r_{l,j}, r_{i,j}) = \left(\frac{\Delta h_{l,j}}{2h_{l,j}}, \frac{\Delta h_{i,j}}{2h_{i,j}} \right) = \left(\frac{h_{i+1,j} - h_{i,j}}{h_{i+1,j} + h_{i,j}}, \frac{h_{i,j+1} - h_{i,j}}{h_{i,j+1} + h_{i,j}} \right). \quad (2.20)$$

Due to the presence of slope factor r , the covariance matrix is not homogeneous horizontally, and the higher the slope factor (the higher the topography gradient), the higher the covariance. This means that the greatest modifications in density and surface elevation are allowed in regions with steep topography gradients, which is consistent with the occurrence of large truncation errors in the horizontal pressure gradient in these regions.

As a first approximation, the model covariance matrix \mathbf{R} is given by

$$\mathbf{R} = \{ \gamma_{\text{geo}}^{-1}, \gamma_{\text{bv}}^{-1} \} \text{Id}, \quad (2.21)$$

and the weights γ_{geo} for the geostrophic constraints and γ_{bv} for the Brunt–Väisälä constraints are chosen so that the maximum modification of the density and surface elevation anomaly is less than a specified value:

$$\begin{cases} |\delta\rho| < \delta\rho_{\text{max}} \\ |\delta\eta| < \delta\eta_{\text{max}}. \end{cases} \quad (2.22)$$

Numerous algorithms are now available to minimize a cost function such as (2.15). For the various experiments shown in the present paper, a preconditioned conjugate gradient algorithm from the Matlab 5.0 sparse system package (Gilbert et al. 1992) has been used on an HP ESS-800 server with 256 megabytes of memory to solve (2.16). The inverse method is iterated a few times to find an optimal value for weight γ .

The removal of the Brunt–Väisälä frequency constraint could be thought to be a great numerical blessing in so far as the optimal problem could then be solved independently for the various σ levels. However, the problem is not that simple and such a simplification leads to real numerical difficulties. The reconstruction of the pressure field from knowledge of its gradient components alone is badly formulated: it is very sensitive to the boundary conditions of the inverse problem along the open frontiers of the domain; the resulting density field shows sharp spurious gradients near the bottom and the numerical problem is ill-conditioned, which leads to severe restrictions on γ_{geo} variations. The use of the Brunt–Väisälä frequency avoids the problem of having to choose the open boundary conditions, preserves the density profile and, just as importantly, leads

TABLE 1. Parameters used in experiment A.

Parameter	Value
Number of grid nodes in the x direction	41
$\Delta x, \Delta y$	20 km
Number of sigma levels	21
$\delta\sigma$	0.05
External mode time step	10 s
Internal mode time step	20 s
Horizontal viscosity	$2000 \text{ m}^2 \text{ s}^{-1}$
Vertical viscosity	$10^{-3} \text{ m}^2 \text{ s}^{-1}$
Coriolis parameter	10^{-4} s^{-1}

to a diagonal dominant optimal system, which is numerically well conditioned.

3. Study of a well-documented configuration (experiment A)

The 2D experiment proposed by MEO is now reviewed in the light of the inverse method just described. It is shown that the spurious truncation current can be decreased by at least one order of magnitude. This 2D experiment was chosen because the amplitude of the truncation errors and the resulting modification in the density field and its Brunt–Väisälä frequency is well documented. It was preferred to the classic seamount studied by Beckman and Haidvogel (1993) and more recently by Mellor et al. (1998) because it is also much closer to the type of problems encountered in coastal oceanography.

The first run is a one-month prognostic run. It provides an evaluation of the truncation error resulting from the use of the classic pressure gradient numerical scheme. For the second run, the pressure gradient was optimized using the inverse method presented in the previous section. The optimized truncation error is shown to have the same order of magnitude as in the experiment by MEO after several months of prognostic running.

The 2D (cyclic) topography and the potential density used can both be found in MEO and are given by

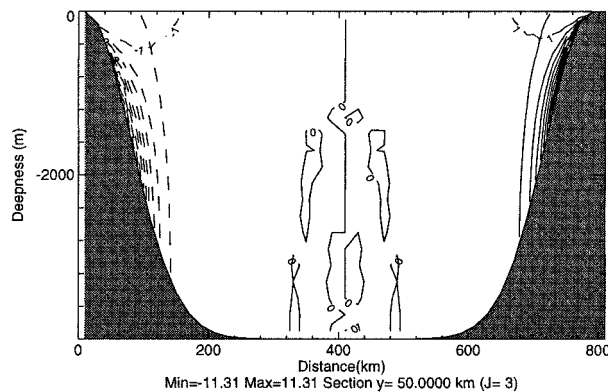


FIG. 3. Experiment A, initial potential alongshelf velocity (cm s^{-1}).

$$h(x, y) = 4000 \left\{ 1 - \exp \left[- \left(\frac{D_x(x, y)}{100 \text{ km}} \right)^2 \right] \right\}, \quad (3.1)$$

where D_x is the distance to the nearest coast. The density and surface elevation fields are initially:

$$\begin{cases} \rho(x^*, y^*, z) = 1000 \left[1.028 - 0.003 \exp \left(\frac{z}{1000 \text{ m}} \right) \right] \\ \eta(x^*, y^*, z) = 0, \end{cases} \quad (3.2)$$

with no initial horizontal gradient. No surface forcing is applied. The same horizontal and vertical grid is also used, with a horizontal spacing of 20 km and 21 sigma levels. The values of the remaining parameters can be found in Table 1.

a. Prognostic run

The horizontal pressure gradient truncation error can be estimated by computing the “potential” geostrophic current error associated with the density distribution (3.2):

$$\begin{cases} u^{\text{err}} = - \frac{1}{\rho_0 f} \frac{\partial P}{\partial y} - u' \\ v^{\text{err}} = \frac{1}{\rho_0 f} \frac{\partial P}{\partial x} - v', \end{cases} \quad (3.3)$$

where pressure P is given by (2.5). This velocity is named “potential geostrophic current error” because (3.3) is a measurement of the truncation error for potential energy that is initially available. Part of this energy is transformed into kinetic energy, giving the truncation error velocity. For the first run, this potential geostrophic current error is given in Fig. 3 with $(u', v') = 0$ since the density profile and surface elevation are horizontally homogeneous. The potential error maximum is located in those regions where the topography gradient is steepest (11.3 cm s^{-1}), and has an antisymmetric structure.

During the first hours of experimentation, the velocity adjusts geostrophically to the pressure gradient truncation error. Then, in the regions of highest velocity, the density field is advected in such a way that the error is removed for velocity (MEO). The resulting modification on the velocity, density anomaly, surface elevation anomaly, and Brunt–Väisälä frequency anomaly after a 1-month run are plotted in Fig. 4. The results are very similar to those obtained by MEO, although we did not study the geostrophic adjustment process and velocity error removal process separately as they did by running the model M diagnostically first. Figure 4a shows that the velocity is already reduced after 1 month to 1.14 cm s^{-1} and surface elevation to 1.9 cm. Meanwhile, the density has adjusted and an anomaly of 0.07 kg m^{-3} is created. The density profile is also mod-

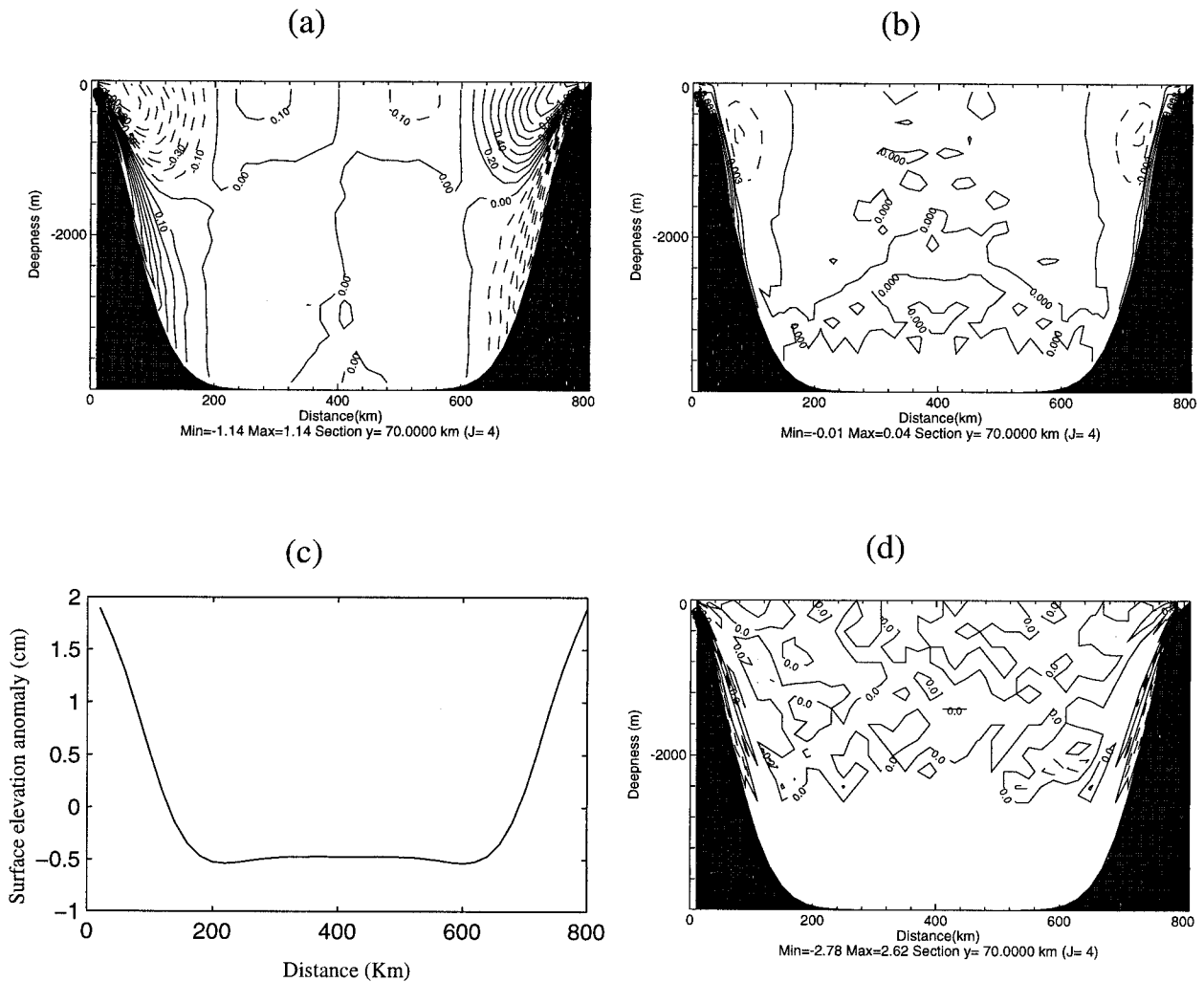


FIG. 4. Experiment A, 30-day prognostic run: (a) alongshelf potential geostrophic current error (cm s^{-1}), (b) density anomaly (kg m^{-3}), (c) surface elevation anomaly (cm), (d) percentage change in the Brunt-Väisälä frequency.

ified and the largest percentage change is equal to 16.6%. The spatial structure of the errors is also very similar to that obtained by MEO. It is antisymmetric and its maximum is reached where the bottom topography gradient is steepest.

If one can afford a one-month spinup, the truncation error can therefore be reduced to about 1 cm s^{-1} , with small changes in the density and surface elevation fields. However, if one wishes to work on short-term simulation, starting, for instance, from in situ measurements, the situation is more critical.

b. Optimized prognostic run

The density field studied in the previous section is used as a first-guess field (\mathbf{x}^b). The computation of the analysis field requires the computation of the solution of a $15\,600 \times 15\,600$ sparse symmetric positive-definite system containing 10% of nonzero elements.

Figure 5 shows the initial optimized truncation error, density, surface elevation, and Brunt-Väisälä frequency change for the second, optimized run. The maximum of the potential geostrophic current error has been reduced to 0.6 cm s^{-1} . This maximum velocity is nearly 20 times smaller than the potential geostrophic current error obtained without optimization (11.3 cm s^{-1}). At the same time, the mean error velocity is reduced by about 50. A very interesting comparison can be made with the results obtained by MEO. The optimized potential geostrophic current error is already one order of magnitude smaller than their geostrophic velocity obtained after 90 days (7 cm s^{-1}), and three times larger than the geostrophic velocity obtained after 2 yr (0.2 cm s^{-1}). The maximum values of the density and percentage change of the Brunt-Väisälä frequency are also very close to those obtained by MEO after a 2-yr run (0.07 and 6%, respectively).

The optimized fields being in a quasi-equilibrium

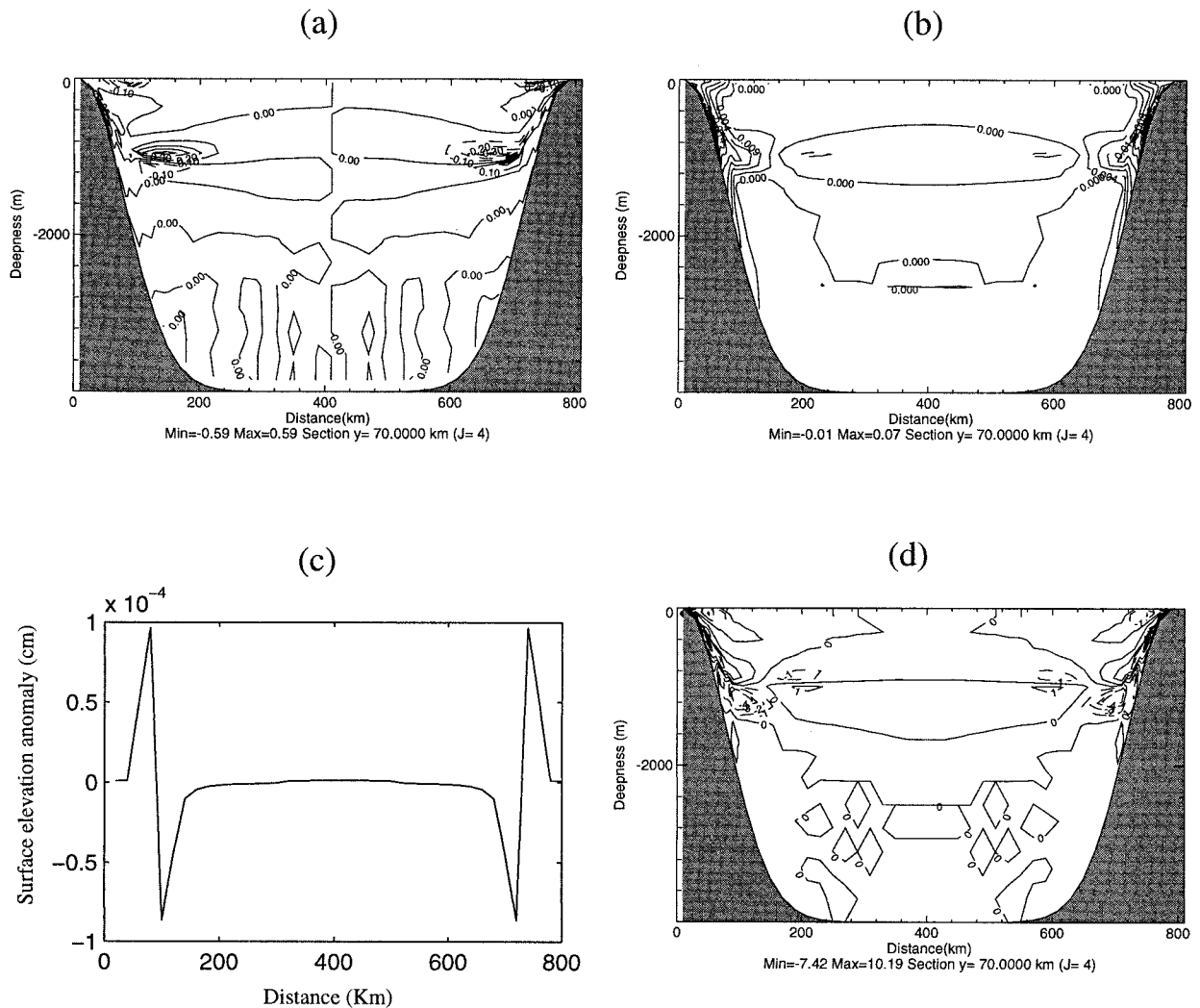


FIG. 5. Experiment A, optimized initial state: (a) alongshelf potential geostrophic current error (cm s^{-1}), (b) density anomaly (kg m^{-3}), (c) surface elevation anomaly (cm), (d) percentage change in the Brunt-Väisälä frequency.

state with respect to the free-surface model M , their magnitude does not change significantly after 1 month of integration (Fig. 6a). The area of the regions affected by the truncation errors is much smaller than in Fig. 4a. The truncation error velocity has been completely removed in the lower layers, particularly in the regions with the steepest topography gradient. The maximum velocity is reached in the upper layers where it is still smaller than in Fig. 4a. The density (Figs. 6b and 6d), and surface elevation (Fig. 6c) are only slightly affected by the truncation error. Figure 7 also provides an interesting comparison of the evolution of the maximum velocity in both experiments over 30 days. It shows that the optimized field maximum error is reduced by one order of magnitude. These rather promising results must however be tempered by the idealized nature of the MEO problem.

Different sensitivity tests were carried out in order to

study the variation in the truncation error with respect to the variation in the maximal density and surface elevation initial disturbance. Results are shown in Table 2. Three analyses were conducted with \mathbf{D} given by (2.19), that is, with a nonhomogeneous horizontal covariance, and then a further three with a homogeneous field, that is, \mathbf{D} is given by

$$\mathbf{D}_{i,j,K} = \{\sigma(\rho), \sigma(\eta)\}. \quad (3.4)$$

We can clearly observe a decrease in the truncation error maximal velocity v_{\max} when the covariance matrix is a function of slope factor r . The nonhomogeneous formulation (2.19) must therefore be preferred to the classic diagonal homogeneous formulation (3.4). This is due to the fact that the truncation errors are clustered in regions of steep bottom topography gradients. Allowing larger modifications of the density and surface elevation fields

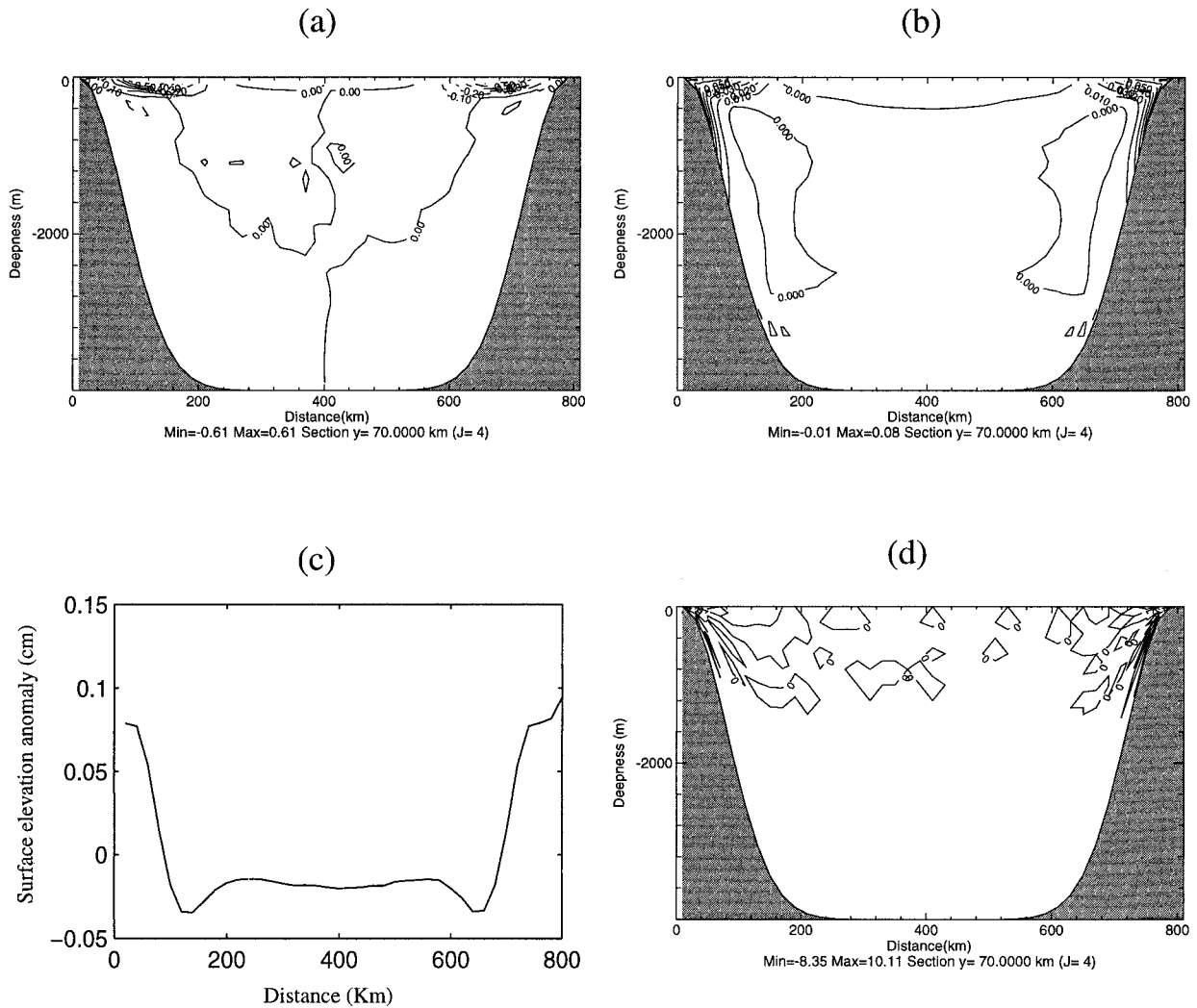


FIG. 6. Experiment A, 30-day optimized prognostic run: (a) alongshelf potential geostrophic current error (cm s^{-1}), (b) density anomaly (kg m^{-3}), (c) surface elevation anomaly (cm), (d) percentage change in the Brunt-Väisälä frequency.

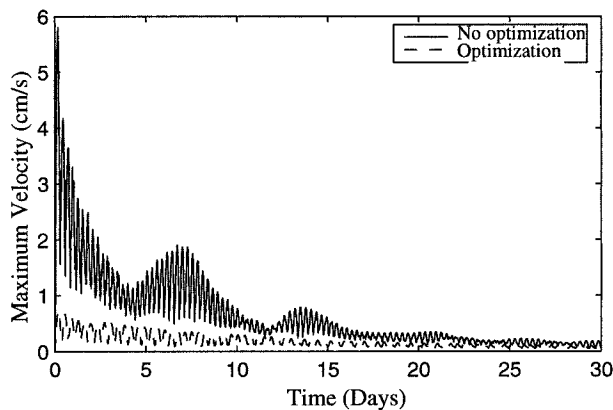


FIG. 7. Experiment A, comparison of the maximum of the potential geostrophic current error for the optimized and nonoptimized fields.

in these regions leads to smaller truncation error maximum velocities.

4. Modeling the western part of the Gulf of Lions

a. Characteristics of the region

The Gulf of Lions in the northwestern Mediterranean offers a large variety of oceanographic processes (see, e.g., Millot 1990). However, their numerical modeling is not straightforward due to severe forcing: steep topography gradients, strong gusts of wind, etc. This region therefore offers a perfect field of investigation for the horizontal pressure gradient truncation error in σ -coordinate systems. The western part of the Gulf of Lions off Roussillon is of particular interest and is studied with a 1.66-km grid and 17 σ levels. The bottom topography is shown in Fig. 8. It was obtained from French Navy maps (SHOM maps). It includes a con-

TABLE 2. Impact of the maximum density and surface elevation modifications on the maximum truncation error for experiment A.

γ	Covariance matrix \mathbf{D}	ρ_{\max} (kg m ⁻³)	η_{\max} (mm)	N_{\max}^2 (%)	v_{\max} (cm s ⁻¹)
10^{-3}	(2.19)	0.070	0.01	8	2.28
2×10^{-4}	(2.19)	.069	0.024	8	1.22
10^{-4}	(2.19)	0.072	0.8	8	0.59
10^{-3}	(3.4)	0.029	0.04	2.26	7.15
2×10^{-4}	(3.4)	0.043	0.07	3.8	5.24
10^{-4}	(3.4)	0.047	0.1	8	3.96

tinental shelf on its northern part followed by a steep continental slope. Along the Cabo Creus (Spain), the absence of continental shelf leads to a sharp slope. Numerically, this part of the gulf is particularly troublesome in so far as iso- σ surfaces vary sharply in the pycnocline.

Figure 8 also shows a vector representation of the slope parameter $\mathbf{r} = (r_{i,j}, r_{i,j})$, given on the C grid by (2.20). The largest values of r can be found along the Catalan and Roussillon coasts where they can reach 0.5. This maximum is a little higher than the maximum value of about 0.4 found by MEO in the North Atlantic.

Three different experiments were conducted. To start with, the density field was supplied by an analytical profile varying linearly both vertically and horizontally (experiment B). In such a case, the geostrophic current can easily be derived analytically, and provides a useful tool to study the validity of (2.10). Experiments C and D were both based on the observations made in the region during the Suivilion experiment (Durrieu de Madron and Panouse 1996). In experiment C, model **M** was initialized with an average depth density profile, whereas in experiment D, real data was interpolated on the model grid and used to compute the spurious truncation errors in a realistic case.

b. Linear density profile (experiment B)

The linear density profile used in experiment B is provided by

$$\rho_{L,J,K} = \rho_{L,1}(I + J) + \rho_{L,2}z, \quad (4.1)$$

where $\rho_{L,1} = 3/[\max(I) + \max(J)]$ and $\rho_{L,2} = 5/2000$. Figure 9 shows two sections of the potential geostrophic current error given by (3.3), the “true” geostrophic current (u^t, v^t) being computed analytically from (4.1). The first section is a cross section of the large slopes in the Cabo Creus region off the Spanish coast and the second section shows both the continental shelf and a cross section of one of the numerous canyons that can be found on the edge of the shelf. The dashed lines show the distribution of the interface σ levels (uniform distribution in experiment C). The errors are uniform vertically. A maximum current of 1.2 cm s⁻¹ is found inside the canyon. This is consistent with (2.10), which predicts such uniform truncation errors with a maximum

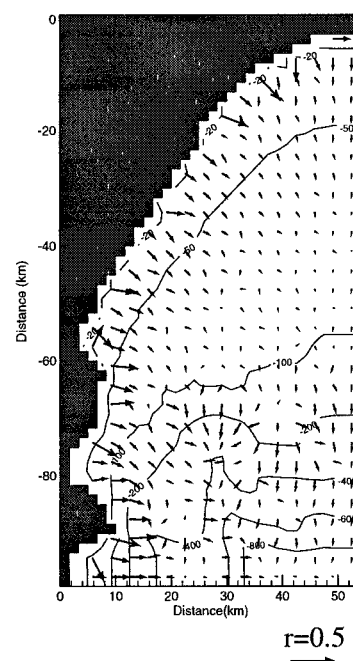


FIG. 8. Bottom topography and slope parameter of the southwestern part of the Gulf of Lions.

of 1.4 cm s⁻¹. This consolidates the idea that a linear profile does not lead to vanishing truncation errors, but gives spurious barotropic currents.

The optimized potential geostrophic current error (Fig. 9b) shows that the error has been reduced to 0.2 cm s⁻¹ and, just as importantly, that the well-organized structures along the lines of constant bottom topography have been removed. A maximum correction of only 1 mm was necessary for surface elevation (Fig. 10). This linear experiment also illustrates the necessity of incorporating the surface elevation gradient in the discussion of the truncation error. A small modification in surface elevation leads in this linear case to the removal of most of the errors, while at the same time, the change in density is obviously small (less than 0.01 kg m⁻³).

c. Homogeneous density field (experiment C)

In experiment C, the density profile is homogeneous and was obtained from the Suivilion experiment (Fig. 11), where the winterlike pycnocline is about 50–70 m deep on the shelf and can reach 100 m at the southeastern edge of the domain. The density field being homogeneous horizontally, no geostrophic currents should theoretically be observed [$u^t, v^t = 0$]. Yet, truncation errors lead to large currents along the continental slope and Fig. 12 shows maximum potential velocity errors of about 23 cm s⁻¹.

To investigate the impact of the slope parameter on the maximum truncation error, the topography gradients were smoothed (see MEO for a description of the iterative filter used), and Table 3 shows how the maxi-

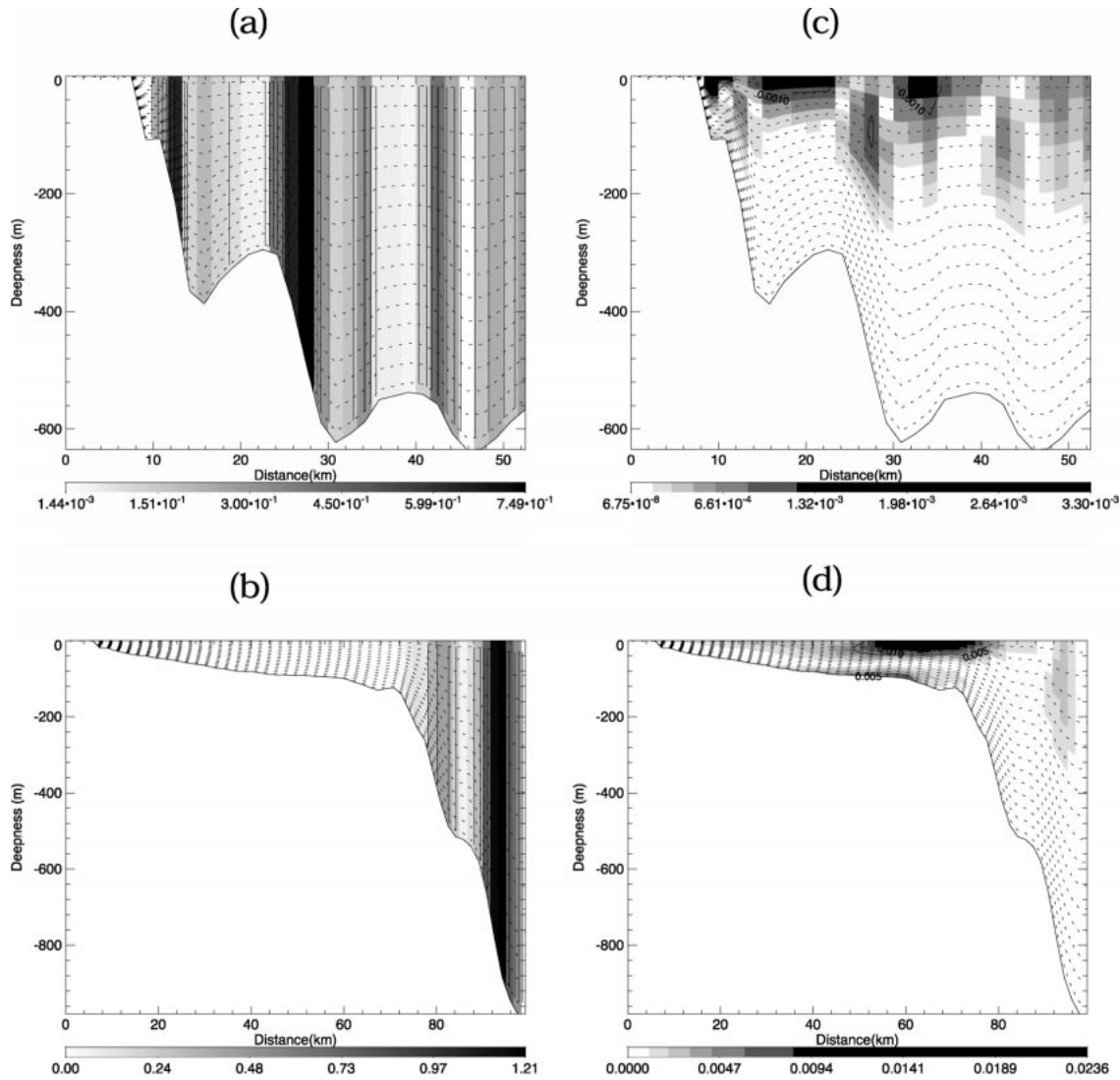


FIG. 9. Experiment B, potential geostrophic current error obtained for a linear density profile: (a) and (b) x and y velocity components without optimization, (c) and (d) x and y velocity components after optimization.

imum geostrophic current behaves depending on slope parameter \mathbf{r} . An obvious observation is that the maximum error increases quickly with \mathbf{r} (up to 22 cm s^{-1} for $\|\mathbf{r}_{\max}\| = 0.5$). Table 3 also provides the percentage of topography points affected by the smoothing of the topography, and it appears that a reduction of $\|\mathbf{r}_{\max}\|$ to 0.3 or even 0.2 only affects a limited number of points (about 5%). Moreover, all the points concerned are located close to the coastline. A value of $\|\mathbf{r}_{\max}\| = 0.2 \text{ cm s}^{-1}$ is thus chosen for the remainder of the study.

The impact of σ -surface distribution is also investigated and Figs. 13a,b show the result of a twofold distribution. This can be compared with the homogeneous distribution (Fig. 12). The thickness of the upper fold of this last distribution is bounded at 100 m, which roughly corresponds to the thickness of the pycnocline (Fig. 11), and is given by

$$h_1 = \min \left[100, \frac{h-100}{160} \right]. \quad (4.2)$$

The distribution of the σ surfaces is then described by

$$K < n_1 \quad \sigma_K = 1 - \frac{n_1 - K + \sigma_A \left[1 - \exp \left(-\frac{K - n_1}{\sigma_B} \right) \right]}{n_1 - 1 + \sigma_A \left[1 - \exp \left(-\frac{1 - n_1}{\sigma_B} \right) \right]}$$

$$K \geq n_1 \quad \sigma_K = \frac{\log[1 + \sigma_C(K - n_1)]}{\log[1 + \sigma_C(N - n_1)]}, \quad (4.3)$$

where n_1 is the number of levels in the lower layer, and σ_A , σ_B , and σ_C are three parameters given by $\sigma_A = 10$, $\sigma_B = 40$, and $\sigma_C = 0.20$.

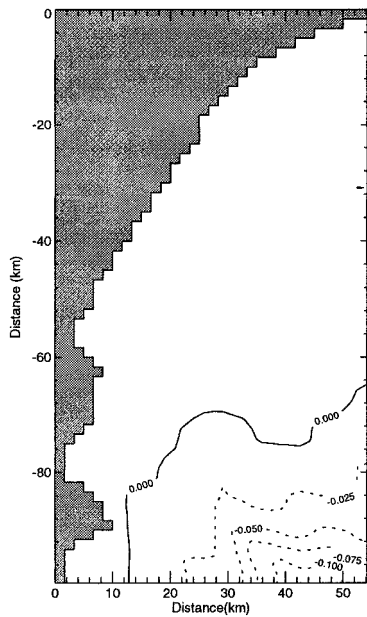


FIG. 10. Experiment B, surface elevation anomaly (cm).

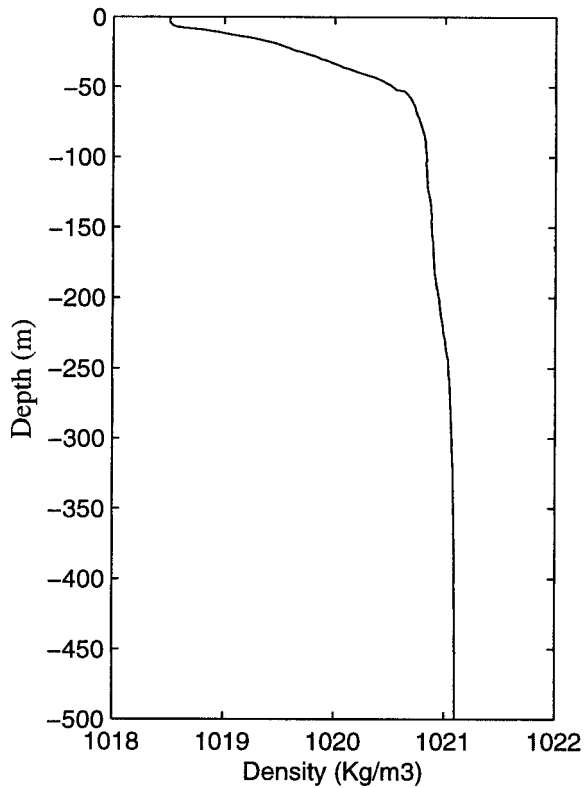


FIG. 11. Horizontal mean density profile from the Suivilion experiment in the Gulf of Lions.

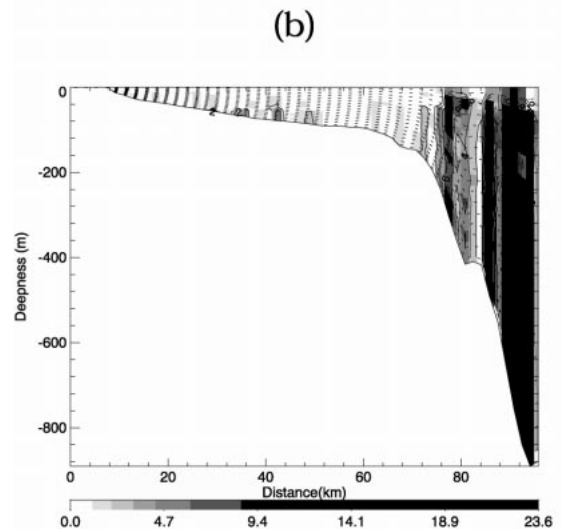
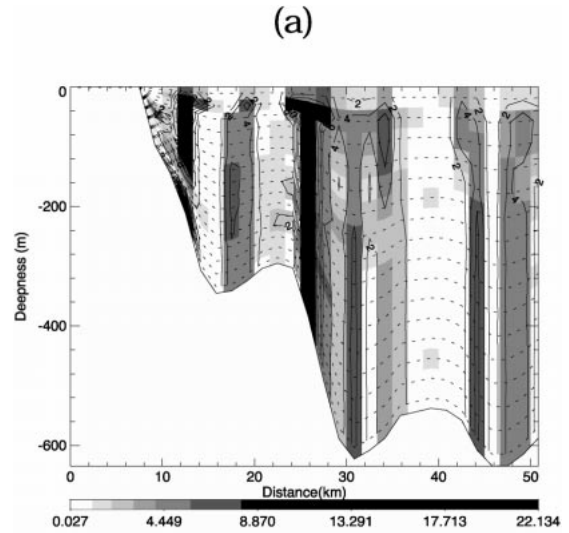


FIG. 12. Experiment C, potential geostrophic current error obtained for a homogeneous density profile using a uniformly spaced σ coordinate: (a) and (b) x and y components without optimization.

The comparison of Figs. 12a,b with Figs. 13a,b shows a substantial reduction in the errors when twofold σ coordinates are used: from 22.1 cm s^{-1} to 9.7 cm s^{-1} in the first section and from 22.6 cm s^{-1} to 5.6 cm s^{-1} in the second section. Indeed, the twofold sigma coordinates provide horizontal σ surfaces in the region of large density variations leading to a better representation of the horizontal pressure gradient (Table 3).

Figures 13c and 13d show the truncation error computed from the “analysis” density, reduced to only a couple of cm s^{-1} . Most of the well-organized patterns of the initial truncation error currents have disappeared. However, due to the modification of the density field, small spurious currents can now be found in the upper fold where the σ surfaces are horizontal. They are lo-

TABLE 3. Influence of the slope parameter (\mathbf{r}) and σ surface distribution on the maximum of the potential geostrophic current error.

$\ \mathbf{r}_{\max}\ $	Modified points (%)	Number of iterations of the filter	u_{\max} (homog. σ)	v_{\max} (homog. σ)	u_{\max} (twofold σ)	v_{\max} (twofold σ)
0.10	24.40	32	22.37	20.83	7.83	7.71
0.15	8.23	14	26.87	21.45	8.17	7.73
0.20	5.00	9	26.87	21.45	9.77	7.23
0.25	3.23	5	26.87	21.45	13.88	7.73
0.30	2.63	2	26.87	21.45	18.33	7.73
0.35	0.91	2	26.87	21.45	17.66	7.73
0.40	0.40	2	26.87	21.45	17.66	8.14
0.45	0.20	2	26.87	21.45	17.66	16.41
0.50	0.00	0	26.87	21.45	17.66	16.41

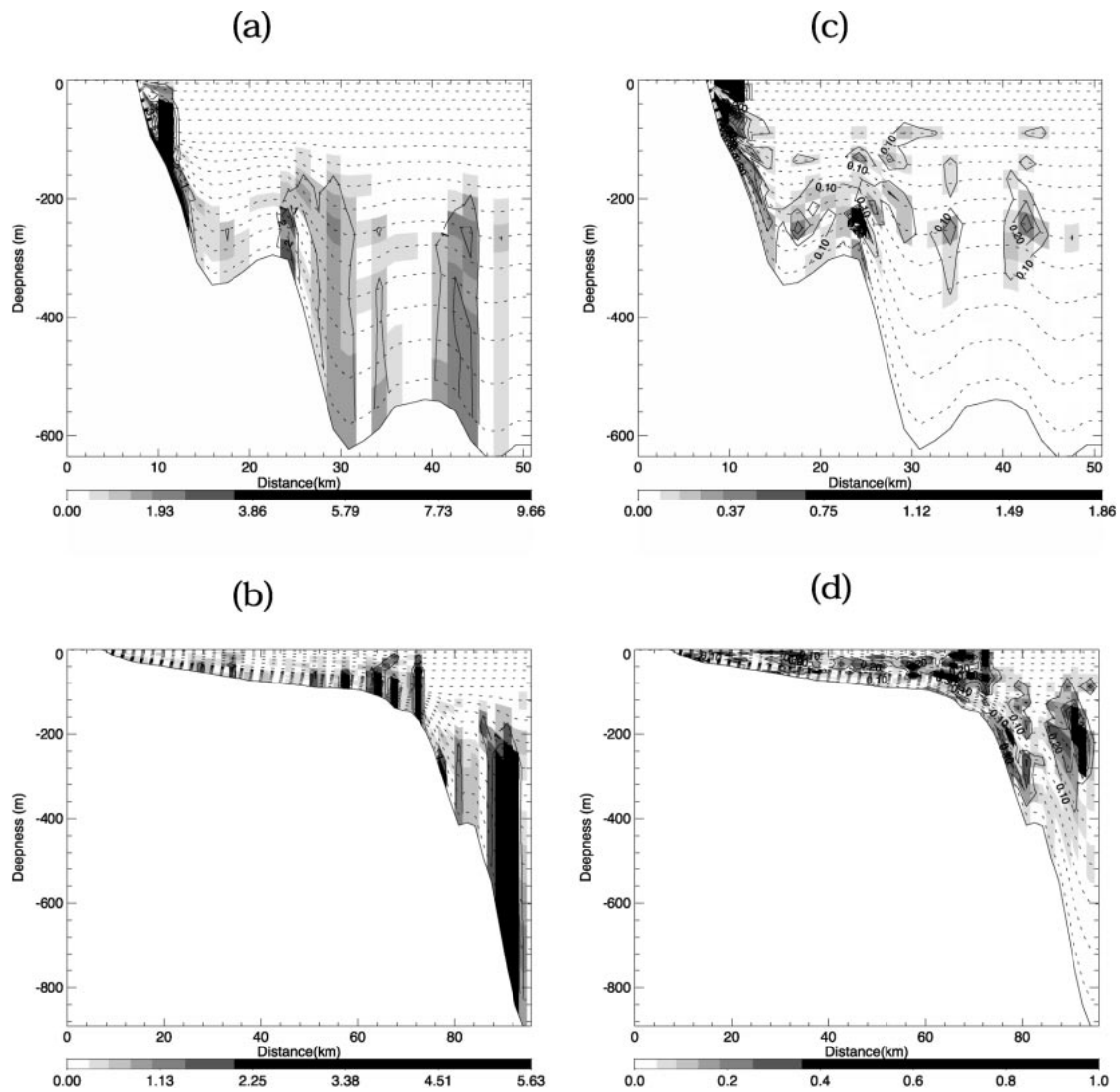


FIG. 13. Experiment C, potential geostrophic current error obtained for a homogeneous density profile using a twofold σ coordinate: (a) and (b) x and y components without optimization, (c) and (d) x and y velocity components after optimization.

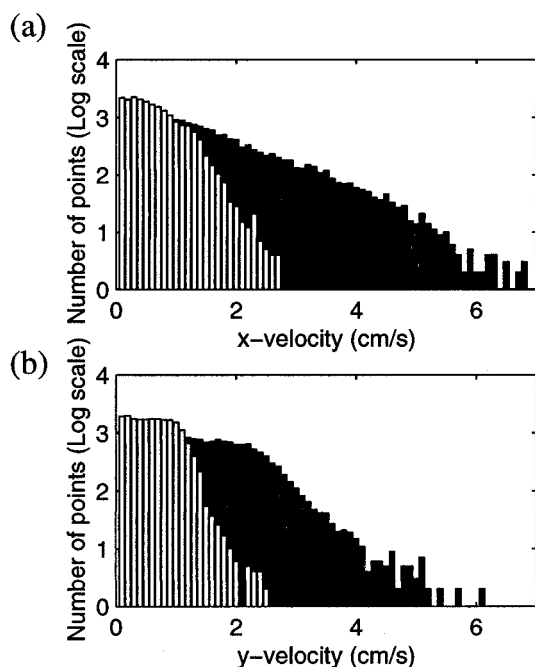


FIG. 14. Experiment C, distribution of the truncation error velocity in the x and y direction after 2 days of diagnostic run. Black: without optimization, white: with optimization.

cated above the region of large initial truncation errors. Indeed, the removal of the truncation errors implies a modification of the density field, which is spread over the water column to conserve the Brunt–Väisälä frequency. The maximum correction of the density and surface elevation fields allowed is 0.07 kg m^{-3} and 1 mm , respectively.

Starting from the first-guess and analysis fields, “twin” diagnostic experiments of 2 days each were conducted. Along the open boundaries, vanishing normal gradient conditions were specified. Figure 14 shows the distribution of the truncation error in the x and y direction at the end of the experiments. The velocities were averaged over an inertial period (about 17 h). For the purposes of this experiment, this distribution was preferred to the evolution of the maximum error, which can “hide” very important discrepancies behind a low maximum value. The distribution obtained with the “analysis” density field exhibits an exponential decrease for increasing amplitude. This is related to the absence of well-organized error structures. On the other hand, the distribution obtained with the first-guess field shows small maxima between 4 and 5 cm s^{-1} , which corresponds roughly to the amplitude of the spurious current flowing along the continental slope.

d. Suivilion density field (experiment D)

For the last experiment (D), the density field from the Suivilion experiment was interpolated on the 1.66-km model grid, the twofold σ -surface distribution being giv-

en by (4.2)–(4.3). Figure 15 shows the observation array of the winter experiment over the whole Gulf of Lions and the position of the model domain. Vertically, observations are made every meter.

A classic Gaussian filter is used for the horizontal interpolation of density (Thiébaux and Pedder 1987). The first-guess density at point (I, J) is given as a function of observed density (y^d) by

$$\mathbf{x}_{I,J}^b = \frac{\sum_{(\alpha,\beta)} \exp\left(-\frac{\xi^2}{\Omega^2}\right) y_{\alpha,\beta}^d}{\sum_{(\alpha,\beta)} \exp\left(-\frac{\xi^2}{\Omega^2}\right)}, \quad (4.4)$$

where ξ is the distance between the model point (I, J) and the observation array point (α, β) , Ω is the smoothing radius, and y^d is the Suivilion observation vector density field. For this experiment, a smoothing radius of 17 km was used to avoid an excessive smoothing of the main structures.

Two vertical interpolations were used to obtain the density field on the coastal model Sigma grid (first-guess density \mathbf{x}^b) (Fig. 16a) and on the z grid whose horizontal levels correspond to observation levels (x^z) (Fig. 16b). Two geostrophic currents are thus obtained from the density fields (\mathbf{x}^b) and (\mathbf{x}^z). The first one is the model geostrophic current computed from the first-guess density and includes the truncation error. The second one is the “true” geostrophic field for the density observations (y^d). From the density field only the vertical shear of the current can be known and, as a consequence, a vanishing current is chosen at the surface of the ocean.

As the vertical density of observations is quite high (one observation every meter), the steplike representation of the bottom topography is considered to be accurate enough for this second geostrophic current to be error free. The magnitude and direction of the horizontal pressure gradient truncation error (3.3) are thus obtained by computing the difference between the model geostrophic current (using \mathbf{x}^b) and the “true” field (u', v'), computed by interpolating the geostrophic current obtained with density \mathbf{x}^z on the model σ grid. Figure 17 shows the true geostrophic current associated with density field \mathbf{x}^z . The signature of the Liguro-Provençal Current can be observed with magnitudes of about 10 cm s^{-1} for a vanishing surface current.

The characteristics of the errors with and without optimization are shown in Fig. 18. For a maximal density and surface elevation disturbance (ρ_{\max} and η_{\max}) equal to 0.09 kg m^{-3} and $2.5 \times 10^{-2} \text{ mm}$, the potential geostrophic current error is reduced to 2 cm s^{-1} . Moreover, as maximum errors are sparse, they are not a major problem for future modeling in so far as the local gradient they create will be quickly diffused. Figure 19 clearly confirms that the optimized field reveals any well-organized current structures: the optimized current histogram (drawn in white) decreases exponentially, al-

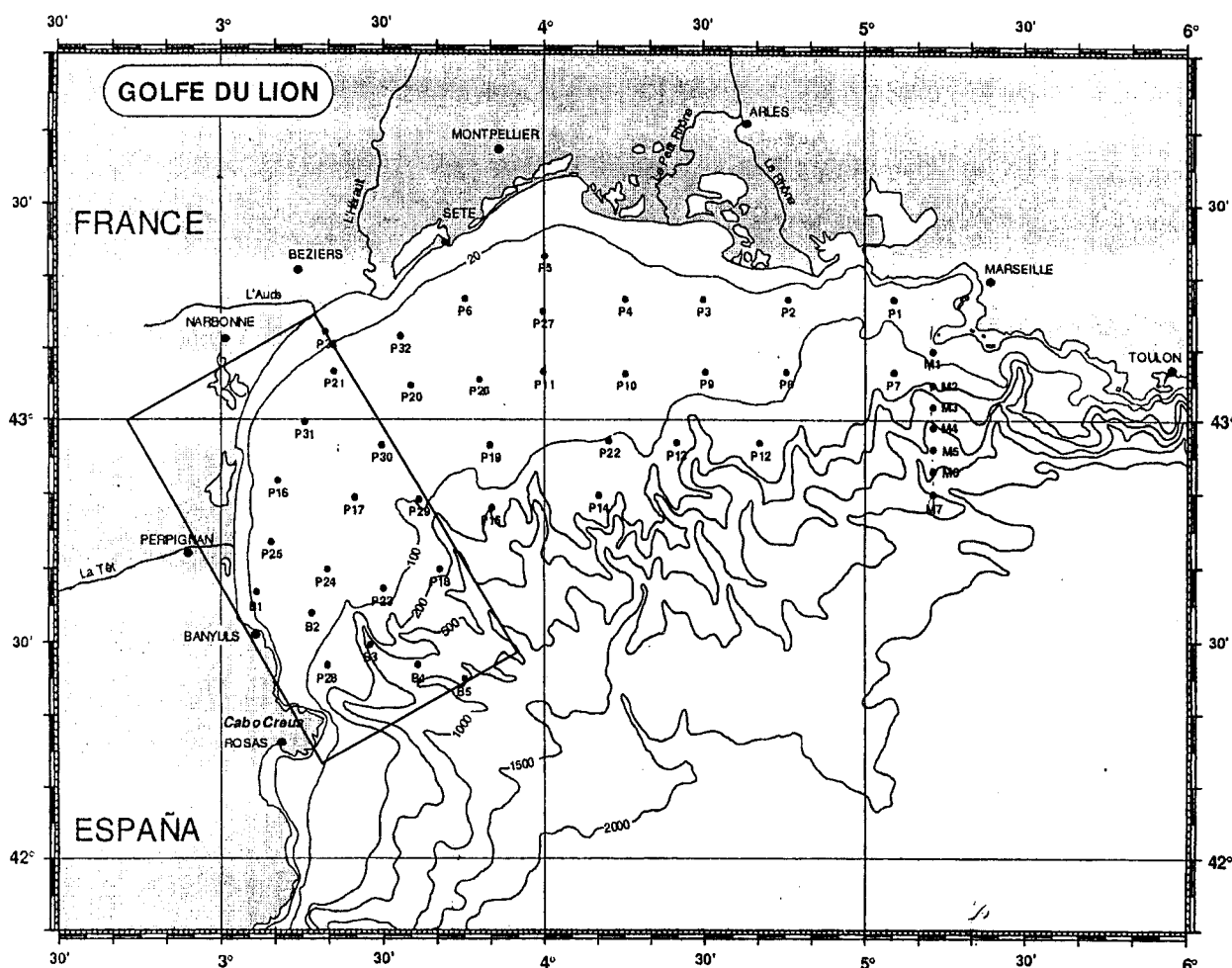


FIG. 15. Observation stations during the Suivilion winter experiment, from Durrieu de Madron and Panouse (1996). Black rectangle: position of the domain studied.

though the nonoptimized histogram (drawn in black) shows, along the shelf, several well-identified structures whose magnitude lies between 6 and 9 cm s^{-1} .

5. Discussion

The various experiments presented so far give an overall picture of the capacity of an inverse method to reduce the horizontal pressure gradient truncation error. This type of error was in fact recognized as a bias of σ coordinate models, and the choice was made to work as accurately as possible with it. The underlying idea is to choose the geostrophic current as the main parameter of the interpolation scheme and, as a consequence, to deduce the pressure (density and surface elevation) from the interpolated geostrophic current. Such ideas were suggested for the atmosphere more than a decade ago by Mesinger and Janjic (1985, p. 109).

We show for well-documented experiment A (MEO) that the initial modification of the density and surface elevation fields by the inverse method was small and

located in the bottom boundary layer along the shelf break. However, the interpolation of the density field in such regions is subject to large errors due in particular to the difficulty in specifying the bottom topography. For instance, the initialization of a coastal model from the outputs of an ocean general circulation model raises the problem of the compatibility of the bottom topographies in the models, and, as a consequence, the interpolation of the density close to the bottom is very often transformed into an extrapolation problem. Thus the adjustment of the density profile in order to give the observed geostrophic current can be seen as an elegant way of avoiding this dangerous extrapolation.

However, the inverse method is only used to decrease the truncation error on the initial horizontal pressure gradient. It implies that this initial horizontal pressure gradient is known with a sufficient accuracy, which is not necessarily the case. For instance, the steplike bottom topography of an ocean general circulation model using z coordinates can lead to large errors on the geostrophic current over the shelf break. Such errors must

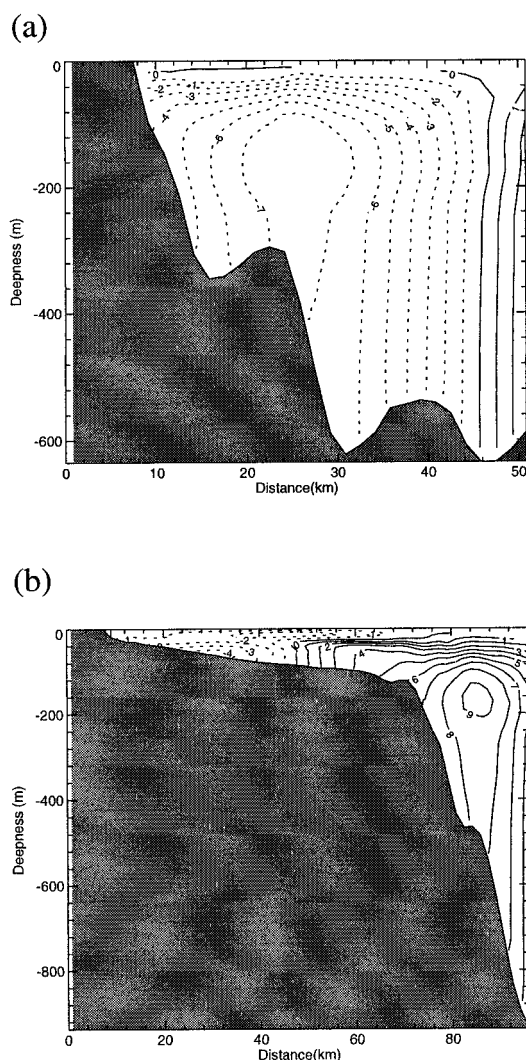


FIG. 16. Suivilion observations: (a) and (b) sections of the baroclinic geostrophic velocity with vanishing surface velocity.

be taken into account and if possible corrected before the large-scale pressure field is used in the inverse method to initialize the coastal model (Auclair 1999). Sparse in situ measurements can also be insufficient to compute the geostrophic current, but if one has a good knowledge of the initial pressure field, the inverse method leads to small errors on the modeling of the corresponding geostrophic current. Yet, it does not reduce other types of errors associated with the use of σ coordinates (e.g., increased diapycnal diffusion, modeling of strongly forced systems, etc.).

In the present paper, we have not developed in detail the minimization of the cost function. We focused on the construction and testing of the cost function (2.15), which reduces the magnitude of the truncation error. The actual optimal problem varies asymptotically like $[(L/\Delta x)^2 N]^4$ where L is the horizontal size of the domain. This is however an asymptotic upper bound of

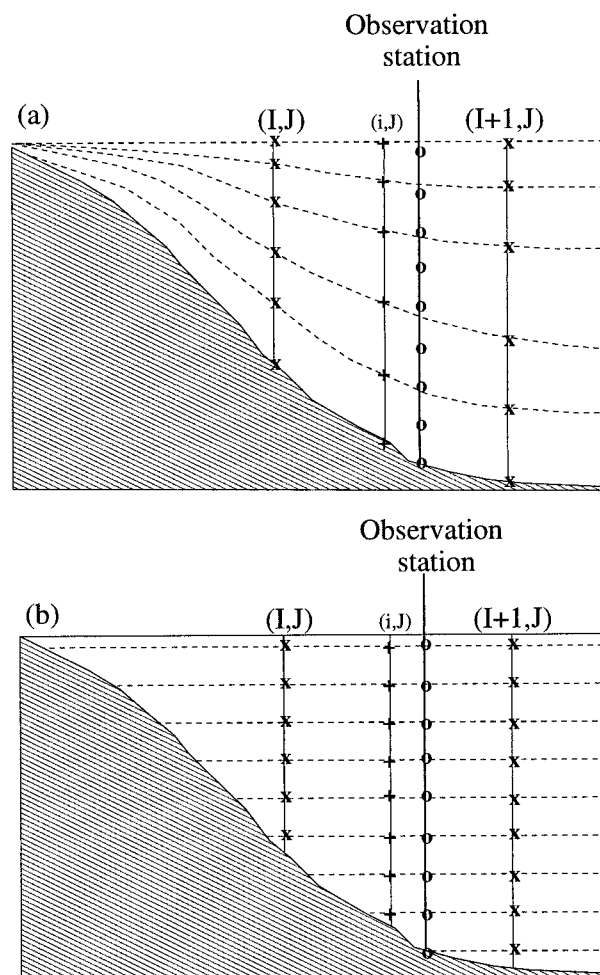


FIG. 17. Vertical interpolation on the σ and z grid: (a) interpolation of the first-guess density x^b on the σ grid, (b) interpolation of the x^c on the z grid, with (O): observation points, (X): density points of the model C grid, (+): velocity points of the model C grid.

the problem, and the use of algorithms for sparse systems leads to drastic improvements. The Suivilion problem leads to the optimization of a $35 \times 60 \times 16$ grid, which necessitates less than 150 megabytes of memory. The same approach has been applied successfully to the optimization of a coastal model initial field near Marseilles (France) involving 30 000 variables on the same 256 megabytes memory machine, the necessary CPU corresponding roughly to a few hour direct simulation over the same domain using the 3D model (Auclair 1999).

The domain can also easily be separated into smaller regions and only the regions located along the shelf break need to be processed. Such a procedure significantly reduces the number of control variables. The minimization of the cost function can also be incorporated into a variational problem when one has access to the adjoint model. As a consequence, there should not be

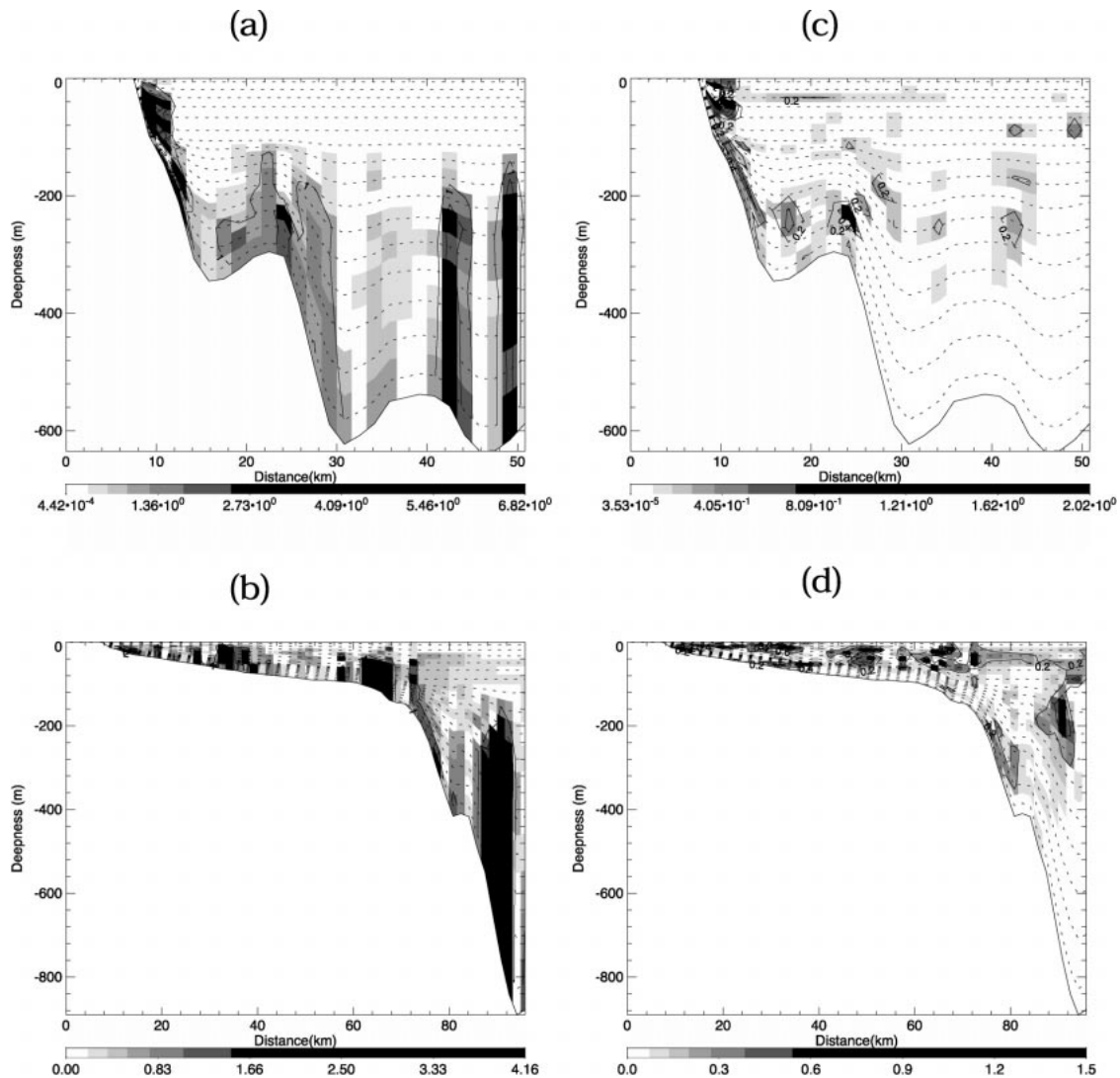


FIG. 18. Experiment D, potential geostrophic current error obtained for the interpolated density field: (a) and (b) x and y velocity components with optimization, (c) and (d) x and y velocity components after optimization.

any computational restrictions to the use of such an inverse method with prognostic model runs.

6. Conclusions

Different solutions have been studied in order to significantly decrease the sigma coordinate truncation error while preserving all the integral pressure gradient constraints: the adjustment of the slope factor, the distribution of the sigma surface, and the use of an inverse technique to adjust the initial density and surface elevation fields.

The decrease in the slope parameter is not in general a good solution in so far as the accuracy of the bottom topography is crucial in coastal modeling. However, we have shown that reducing this parameter from 0.5 to 0.2 results in the truncation error being reduced by about 50,

while only a few sparse topography points along the coastline were affected. As a matter of fact, higher values for the slope parameter do not offer a more realistic bottom topography, but result in much higher discrepancies in the computation of the horizontal pressure gradient.

The twofold sigma coordinate also has a very positive impact on the magnitude of the truncation error. Indeed, it provides horizontal σ surfaces in the upper part of the ocean, that is, in regions of high vertical density gradients. It also has a very positive impact on spurious diapycnal diffusion.

Last, we have shown that an appropriate inverse technique was an efficient way of significantly reducing the truncation error. The maximal disturbance of the density and surface elevation fields was less than 0.2 kg m^{-3} and 1 mm. It is also very interesting to observe that the resulting truncation errors after optimization are sparse

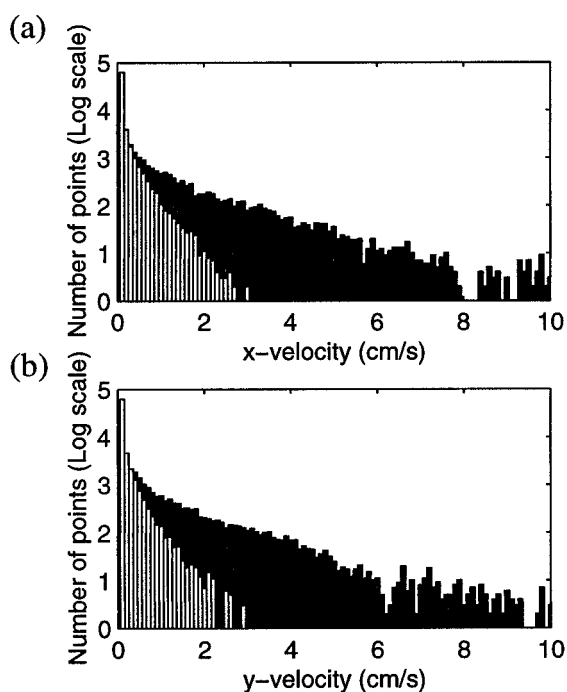


FIG. 19. Experiment D, distribution of the potential truncation error velocity in the x and y direction, black: without optimization, white: after optimization.

and are not found in well-organized structures above the shelf break. As a consequence, they are more easily destroyed by diffusion as time goes on. Experiment A also showed that the density and surface elevation disturbance is of the same order of magnitude as the disturbance obtained after a month of prognostic modeling by MEO. The computation of an optimized field avoids long spinup periods and reduces the second-order truncation error, which cannot be decreased by advection.

Acknowledgments. This study was supported by EP-SHOM under Contract EPSHOM/CNRS 27/95, the Programme National d'Océanologie Côtière, the Programme Atmosphère et Océan à Moyenne échelle, and was undertaken in the framework of the MAST-III-ELOISE European Union METRO-MED Project (Dynamics of Matter Transfer and Biochemical Cycles: Their Modeling in Coastal Systems of the Mediterranean Sea). We acknowledge the support of the European Commission's Marine Science and Technology program under Contract CT 960049. We gratefully thank Xavier Durrieu de Madron (CEFREM, Perpignan) for the Suivilion data. Finally, we would like to thank Serge Prieur for his technical support.

REFERENCES

- Arakawa, A., and V. R. Lamb, 1977: Computational design of the basic dynamical processes of the UCLA general circulation model. J. Chang, Ed., Vol. 17, *Method in Computational Physics*, Academic Press, 173–265.
- , and M. J. Suarez, 1983: Vertical differencing of the primitive equations in sigma coordinates. *Mon. Wea. Rev.*, **111**, 34–45.
- Auclair, F., 1999: Modélisation océanographique côtière: Initialisation et forçage. Ph.D. dissertation, l'Université Paul Sabatier, 155 pp. [Available from Université P. Sabatier, 118 Route de Narbonne, 31062 Toulouse Cedex 4, France.]
- Barnier, B., P. Marchesiello, A. Pimenta De Miranda, and J.-M. Molines, 1998: A sigma-coordinate primitive equation model for studying the circulation in the South Atlantic. Part I: Model configuration with error estimates. *Deep-Sea Res. I*, **45**, 543–572.
- Beckers, J. M., 1995: La méditerranée occidentale: De la modélisation mathématique à la simulation numérique. Ph.D. dissertation, Université de Liège, 342 pp. [Available from Institut de Chimie, Bât B6, Sart Tilman, B-4000 Liège, Belgium.]
- Beckmann, A., 1998: The representation of bottom boundary layer processes in numerical ocean circulation models. *Ocean Modeling and Parameterization*, E.P. Chassignet and J. Verron, Eds., NATO Science Series C: Mathematical and Physical Sciences, Vol. 516, Kluwer Academic, 451 pp.
- , and D. B. Haidvogel, 1993: Numerical simulation of flow around a tall isolated seamount. Part I: Problem formulation and model accuracy. *J. Phys. Oceanogr.*, **23**, 1736–1753.
- , and —, 1997: A numerical simulation of flow at Fieberling Guyot. *J. Geophys. Res.*, **102** (C3), 5595–5613.
- Blumberg, A. F., and G. L. Mellor, 1987: A description of a three-dimensional coastal ocean circulation model. Three-Dimensional Coastal Ocean Models, N. S. Heaps, Ed., Coastal and Estuarine Sciences Series, Vol. 4, Amer. Geophys. Union.
- Chu, P. C., and C. Fan, 1997: Sixth-order difference scheme for sigma coordinate ocean models. *J. Phys. Oceanogr.*, **27**, 2064–2071.
- Corby, G. A., A. Gilchrist, and R. L. Newson, 1972: A general circulation model of the atmosphere suitable for long period integrations. *Quart. J. Roy. Meteor. Soc.*, **98**, 809–832.
- Deleersnijder, E., and J. M. Beckers, 1992: On the use of the s -coordinate system in regions of large bathymetric variations. *J. Mar. Syst.*, **3**, 381–390.
- Durrieu de Madron, X., and M. Panouse, 1996: Transport de matière particulaire en suspension sur le plateau continental du Golfe du Lion. Situation estivale et hivernale. *C. R. Acad. Sci. Paris*, **322**, 1061–1070.
- Estournel, C., V. Kondrachoff, P. Marsaleix, and R. Vehil, 1997: The plume of the Rhone: Numerical simulation and remote sensing. *Contin. Shelf Res.*, **17**, 899–924.
- Gary, J. M., 1973: Estimate of truncation error in transformed coordinate, primitive equation atmospheric models. *J. Atmos. Sci.*, **31**, 255–281.
- Gerdes, R., 1993: A primitive equation model using a general vertical coordinate transformation. Part 1: Description and testing of the model. *J. Geophys. Res.*, **98**, 14 683–14 701.
- Gilbert, J. R., C. Mooler, and R. Schreiber, 1992: Sparse matrices in Matlab: Design and implementation. *SIAM J. Matrix Anal. Appl.*, **13**, 333–356.
- Gill, A. E., 1982: *Atmosphere–Ocean Dynamics*. International Geophysics Series, Vol. 30, Academic Press, 662 pp.
- Haney, R. L., 1991: On the pressure gradient force over steep topography in sigma coordinate ocean models. *J. Phys. Oceanogr.*, **21**, 610–619.
- Ide, K., P. Courtier, M. Ghil, and A. C. Lorenc, 1997: Unified notation for data assimilation: Operational, sequential and variational. *J. Meteor. Soc. Japan*, **75**, 181–189.
- Marsaleix, P., C. Estournel, V. Kondrachoff, and R. Vehil, 1998: A numerical study of the formation of the Rhône river plume. *J. Mar. Syst.*, **14**, 99–115.
- McCalpin, J. D., 1994: A comparison of second-order and fourth-order pressure gradient algorithms in σ -coordinate ocean model. *Int. J. Numer. Methods Fluids*, **128**, 361–383.
- Mellor, G. L., T. Ezer, and L. Y. Oey, 1994: The pressure gradient conundrum of sigma coordinate ocean models. *J. Atmos. Oceanic Technol.*, **11**, 1126–1134.
- , L.-Y. Oey, and T. Ezer, 1998: Sigma coordinate pressure gra-

- dient errors and the seamount problem. *J. Atmos. Oceanic Technol.*, **15**, 1112–1131.
- Mesinger, F., and Z. I. Janjic, 1985: Problems and numerical methods of the incorporation of mountains in atmospheric models. *Lect. Appl. Math.*, **22**, 81–120.
- Millot, C., 1990: The Gulf of Lions' hydrodynamics. *Contin. Shelf Res.*, **10**, 885–894.
- Song, Y., and D. B. Haidvogel, 1994: A semi-implicit ocean circulation model using a generalized topography-following coordinate. *J. Comput. Phys.*, **115**, 228–244.
- Thiébaux, H. J., and M. A. Pedder, 1987: *Spatial Objective Analysis with Applications in Atmospheric Science*. Academic Press, 299 pp.
- Wabha, G., and J. Wendelberger, 1980: Some new mathematical methods for variational objective analysis using splines and cross validation. *Mon. Wea. Rev.*, **108**, 1122–1143.